

See discussions, stats, and author profiles for this publication at: <https://www.researchgate.net/publication/264117244>

Mesoporous Co₃O₄ with Controlled Porosity: Inverse Micelle Synthesis and High-Performance Catalytic CO Oxidation at -60 °C

ARTICLE in CHEMISTRY OF MATERIALS · JULY 2014

Impact Factor: 8.35 · DOI: 10.1021/cm502106v

CITATIONS

15

READS

123

6 AUTHORS, INCLUDING:



[Yongtao Meng](#)

University of Connecticut

27 PUBLICATIONS 151 CITATIONS

[SEE PROFILE](#)



[Zheng Ren](#)

University of Connecticut

24 PUBLICATIONS 235 CITATIONS

[SEE PROFILE](#)



[Sheng-Yu Chen](#)

University of Connecticut

10 PUBLICATIONS 205 CITATIONS

[SEE PROFILE](#)



[Steven L Suib](#)

University of Connecticut

653 PUBLICATIONS 15,565 CITATIONS

[SEE PROFILE](#)

Mesoporous Co_3O_4 with Controlled Porosity: Inverse Micelle Synthesis and High-Performance Catalytic CO Oxidation at -60°C

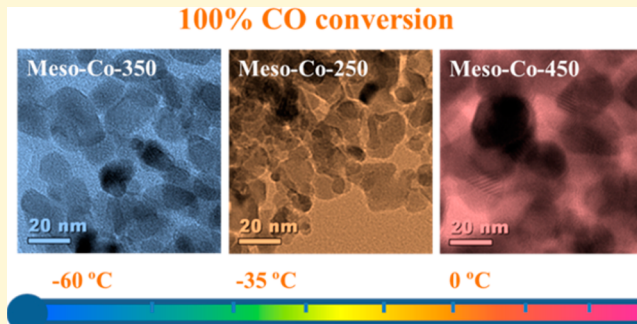
Wenqiao Song,[†] Altug S. Poyraz,[†] Yongtao Meng,[†] Zheng Ren,[‡] Sheng-Yu Chen,[†] and Steven L. Suib*,^{†,‡}

[†]Department of Chemistry, University of Connecticut, U-3060, 55 North Eagleville Road, Storrs, Connecticut 06269, United States

[‡]Institute of Materials Science, University of Connecticut, U-3060, 91 North Eagleville Road, Storrs, Connecticut 06269, United States

Supporting Information

ABSTRACT: Crystalline mesoporous cobalt oxides with improved catalytic activity in CO oxidation were synthesized using an inverse surfactant micelle method. The prepared materials are monodispersed nanoparticle aggregates, and the mesopores are formed by connected intraparticle voids. Powder X-ray diffraction (PXRD), N_2 sorption, field emission scanning electron microscope (FE-SEM) and high-resolution transmission electron microscopy (HR-TEM) revealed that both pore and nanoparticle sizes are enlarged with increasing thermal treatment temperatures ($150\text{--}450^\circ\text{C}$). Mesoporous cobalt oxide calcined at 350°C exhibited the best oxidation activity and can achieve complete oxidization (100% conversion) of CO to CO_2 at -60°C under normal conditions ($\sim 3\text{--}10\text{ ppm of H}_2\text{O}$) and at 80°C under moisture rich conditions ($\sim 3\text{ H}_2\text{O}$). The commercial Co_3O_4 reached 100% conversion at 220°C under normal conditions. X-ray photoelectron spectroscopy (XPS), O_2 -temperature-programmed desorption ($\text{O}_2\text{-TPD}$), H_2 -temperature-programmed reduction ($\text{H}_2\text{-TPR}$), CO-TPD, and N_2 sorption analyses indicated that the surface oxygen vacancy and large surface area promoted the lattice oxygen mobility of the catalysts and further enhanced their catalytic performance. The catalysts were deactivated by accumulation of water and formation of carbonates, but their activities can be easily restored by expelling water and carbonates at moderate temperature (200°C).



1. INTRODUCTION

The oxidation of carbon monoxide (CO) to carbon dioxide (CO_2) has been extensively studied for the past decades due to its many potential applications in air purification, automobile exhaust gas treatment, purifying H_2 in polymer electrolyte fuel cells, closed-cycle CO_2 lasers, and CO gas sensors.^{1–4} Moreover, in practical application, especially automotive emission control, large amounts of CO are usually generated during the cold start period, which causes serious environmental problems. Therefore, it is of great necessity to regulate the CO emission by developing efficient catalysts that convert CO into CO_2 at relatively low temperatures. In the past 2 decades, noble metals have been discovered to function as high-performance oxidation catalysts for various industrial relevant reactions including CO oxidation and the reaction temperature for complete oxidation has been significantly reduced. Haruta et al. was the first to report total conversion of CO oxidation at temperatures as low as -70°C by using supported gold nanoparticles.⁵ However, their high cost and scarcity make noble metal catalysts less desirable. A great deal of research has thus been devoted to search and develop cost-effective catalysts which are noble metal free but are able to deliver comparable catalytic performances. Transition metal or composite transition metal oxides represent promising candidates since they

are cheap, earth abundant, and capable of low temperature catalytic conversion.^{2,6–8} Among these, Co_3O_4 stands out due to its high activity for CO oxidation at temperatures far below room temperature.

Considerable work has been done toward low temperature CO oxidation over Co_3O_4 based materials. Thormahlen et al.² prepared an aluminum supported Co_3O_4 catalyst, which exhibited a light off temperature T_{50} of -63°C after a preoxidation step. Xie et al.⁶ synthesized Co_3O_4 nanorods with predominantly exposed $\{110\}$ planes, which can completely oxidize CO to CO_2 at -77°C under a normal feed gas. Jia et al.⁹ reported low temperature CO oxidation under normal conditions with 100% conversion at -76°C achieved by using $\text{Co}_3\text{O}_4\text{-SiO}_2$ nanocomposites. However, these catalysts need to be activated in oxidizing atmospheres at relatively high temperatures ($>350^\circ\text{C}$) prior to catalytic tests. Pretreatment in an oxidizing atmosphere has a chance of partially oxidizing the catalyst¹⁰ and the preadsorbed labile O_2 on the catalyst surface can enhance the oxidation of CO at low temperatures. Therefore, the catalytic performance of the catalysts cannot be

Received: June 9, 2014

Revised: July 15, 2014



truly revealed. One drawback of Co_3O_4 based catalysts for CO oxidation is their low water tolerance. They are quickly deactivated by the presence of moisture in the gas stream, thus placing a new demand for highly active moisture tolerant catalysts. Several attempts were made to solve this problem, including polydimethylsiloxane (PDMS) coating of the oxide surface¹¹ and incorporation of CeO_2 .¹² Nevertheless, the activity under moisture rich conditions is still far lower than those under normal or dry conditions. Therefore, the design for noble metal free hydrophobic catalysts still remains a challenge.

Since the pioneering work of Mobil Oil researchers,¹³ mesoporous materials have attracted tremendous attention in many different catalytic systems such as catalysis, sorption, gas sensors, and optics. Their catalytic activities have been reported to exceed their nonporous counterparts due to their high surface area, nanocrystallinity, mesoporosity, and pore volume.^{14–16} Mesoporous transition metal oxides such as Fe, Co, and Mn oxides have been given particular attention due to their stable multiple oxidation states, yielding numerous oxides of the same material. However, these materials have weak inorganic–surfactant interactions, which make the synthesis of mesoporous structures of these materials difficult by conventional approaches.¹⁷ Recently, our group has successfully synthesized a series of mesoporous materials, which are named UCT materials (University of Connecticut mesoporous materials).¹⁸ Instead of conventional approaches, an inverse surfactant (Pluronic, P123) micelle was used as the soft template to create the mesopores. The sol–gel process was controlled by unique NOx chemistry. Subsequently treating the materials with different heating cycles yielded monomodal, thermally controlled mesoporous materials with crystalline walls. Specifically, herein we report the preparation of mesoporous Co_3O_4 (UCT-8), which is difficult to produce using conventional methods,¹⁹ and use as a highly active catalyst for low temperature CO oxidation. The synthesized mesoporous Co_3O_4 showed promising activity in CO oxidation under both normal conditions ($\sim 3\text{--}10$ ppm of H_2O) and moisture rich conditions ($\sim 3\%$ H_2O). Mild pretreatment conditions under an inert atmosphere at 200 °C and low oxygen content (1%) were used. The materials were characterized by powder X-ray diffraction (PXRD), N_2 sorption, X-ray photoelectron spectroscopy (XPS), high-resolution-transmission electron microscopy (HR-TEM), H_2 -temperature-programmed reduction (TPR), and temperature-programmed reduction (TPD) to examine the effect of heating cycles on the material properties. The effects of surface lattice defects and surface areas on the catalytic activity are discussed in detail.

2. EXPERIMENTAL SECTION

2.1. Catalysts Synthesis. All chemicals used were reagent-grade. Cobalt(II) nitrate hexahydrate ($\text{Co}(\text{NO}_3)_2 \cdot 6\text{H}_2\text{O}$, ≥98.0), 1-butanol (anhydrous, 99.8%), and poly(ethylene glycol)-block-poly(propylene glycol)-block-poly(ethylene glycol) PEO₂₀–PPO₇₀–PEO₂₀ (Pluronic P123) were purchased from Sigma-Aldrich. Concentrated nitric acid (68%–70% HNO_3) was purchased from J. T. Baker. To synthesize the mesoporous Co_3O_4 , 5 g (0.017 mol) of $\text{Co}(\text{NO}_3)_2 \cdot 6\text{H}_2\text{O}$ was dissolved in a solution containing 17 g (0.33 mol) of 1-butanol, 2.4 g (0.038 mol) of HNO_3 , and 2.5 g (4.31×10^{-4} mol) of P123 in a 400 mL beaker. After magnetic stirring at room temperature, a clear gel was formed. The clear gel was then placed in an oven at 120 °C for 3.5 h. The obtained powder was washed with ethanol several times, centrifuged, and dried in a vacuum oven. The powders were calcined at 150 °C for 12 h (designated UCT-7) and further heated to 250 °C,

350 °C, and 450 °C, respectively, for 1 h with a heating rate of 1 °C/min (designated UCT-8). All the heating cycles were done under air. Samples were nominated as Meso-Co-X (X = 150, 250, 350, and 450), representing samples heat treated at 150 °C, 250 °C, 350 °C, and 450 °C, respectively. Commercial Co_3O_4 (C– Co_3O_4) from Strem Chemical Inc. was 99.5% in purity and used as received.

2.2. Materials Characterization. Powder X-ray diffraction analyses were performed on a Rigaku Ultima IV diffractometer with Cu $\text{K}\alpha$ radiation ($\lambda = 1.5406 \text{ \AA}$) at room temperature. The operating voltage was 40 kV, and the current was 40 mA. Both low angle ($2\theta = 0.5\text{--}8^\circ$) and wide angle ($2\theta = 5\text{--}75^\circ$) diffraction patterns were measured. N_2 sorption measurements were performed on a Quantachrome Autosorb-1-1C automated sorption system. The samples were degassed at 200 °C for 4 h (120 °C, 4 h for UCT 7) prior to the experiments. The surface areas were calculated by the Brunauer–Emmett–Teller (BET) method, and the pore size distributions were obtained by the Barrett–Joyner–Halenda (BJH) method from the desorption branch of the isotherms. The morphologies of the samples were investigated with a Zeiss DSM 982 Gemini field emission scanning electron microscope (FE-SEM) with a Schottky emitter at an accelerating voltage of 2.0 kV and a beam current of 1.0 mA. Samples were dispersed in methanol and mounted on silicon wafers. High-resolution transmission electron microscopy (HR-TEM) images were collected by a JEOL 2010 FasTEM microscope operating at 200 kV. The samples were prepared by using a focused-ion-beam (FIB) technique to make them thin enough to be observed by HRTEM. The X-ray photoelectron spectroscopy (XPS) analyses were conducted on a PHI model 590 spectrometer with multiprobes (Physical Electronics Industries Inc.). Al– $\text{K}\alpha$ radiation ($\lambda = 1486.6 \text{ eV}$) was used as the radiation source. Fourier transform-infrared spectroscopy (FT-IR) were collected using a Nicolet Magna 560 spectrometer equipped with a TGS detector. A total of 64 scans were collected at 4 cm^{-1} spectral resolution. Pellets were made by diluting samples in KBr.

Temperature-programmed mass spectrometry analyses were conducted in a programmable tube furnace equipped with a gas analyzer MKS coupled with a quadruple mass selective detector. About 100 mg (200 mg for O_2 -TPD) of materials were packed in a quartz tube reactor mounted into the tube furnace. The loaded samples were pretreated in an inert gas flow (Ar) at 200 °C for 1 h to clean the catalyst surface before each test. Temperature-programmed measurements were performed from room temperature to 800 °C with a heating ramp rate of 10 °C/min. In H_2 -TPR measurements, 10% H_2 / N_2 flow was passed through the catalyst bed at a flow rate of 50 sccm, while the temperature was ramped from room temperature (RT) to 600 °C. In CO -TPD measurements, samples were first exposed to 10% CO/He at room temperature for 1 h. Then the samples were purged with Ar for 30 min to remove any surface physisorbed gases and residual feed gas from the streams. After purging, the samples were heated under argon flow from RT to 600 °C. By replacing the 10% CO/He with pure O_2 , O_2 -TPD was conducted from RT to 800 °C. The flow rate was 200 sccm. TPD measurements under inert atmosphere after deactivation were also measured. The reaction gas mixture (1% CO , 1% O_2/N_2) was passed through the catalyst bed with 200 sccm flow rate for 15 h to ensure complete deactivation. Subsequently, the catalyst was purged with argon for 30 min to remove any residual gases. After that, the sample was heated from room temperature to 600 °C under an Ar flow (200 sccm).

2.3. Catalytic Tests. CO oxidation was carried out in a continuous flow fixed bed quartz tubular reactor under atmospheric pressure. About 100 mg of as-prepared catalyst was used for each test. Before the measurement, the catalysts were pretreated under helium flow (15 sccm) for 1 h at 200 °C (120 °C for UCT-7) to clean the catalyst surface. After cooling down, a gas mixture of 1% CO, 1% O_2 balanced in N_2 was passed through the catalyst bed with a flow rate of 20 sccm. The outlet gas streams were analyzed by an online gas chromatograph (SRI 8610C Multiple Gas Analyzer No. 1 GC) equipped with a thermal conductivity detector (TCD), a 6 foot long molecular sieve 13X packed column, and a 6 foot long silica gel packed column. The reaction temperature was measured using a K-type thermocouple

inserted directly into the catalyst bed. Temperatures below 0 °C were achieved by mixing dry ice and ethanol in a Dewar flask. GC samples were injected after 10 min stabilization at any given temperature. The reaction conversion was calculated based on the CO concentration, and N₂ was used as an internal standard. Normal condition (~3–10 ppm of H₂O) was obtained by using the as-mixed normal feed gas. Moisture rich condition was obtained by passing the feed gas through a water bubbler at room temperature (~3% water vapor).

3. RESULTS

3.1. Physicochemical Properties. 3.1.1. PXRD and TEM.

Figure 1 shows both high (a) and low angle (b) PXRD patterns

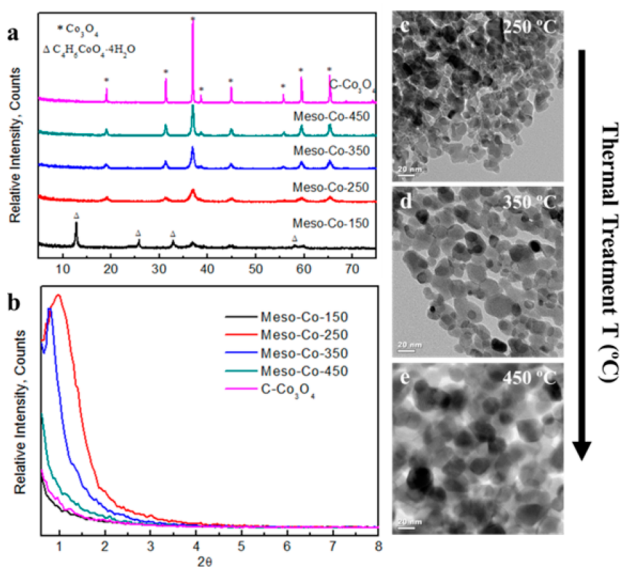


Figure 1. Characterizations of as-prepared materials: (a) low angle and (b) wide angle PXRD patterns of Meso-Co-X (X = 150, 250, 350, and 450) and commercial Co₃O₄ (C-Co₃O₄) samples. TEM images of (c) Meso-Co-250, (d) Meso-Co-350, and (e) Meso-Co-450 showing particle growth (scale bar, 20 nm).

of mesoporous cobalt oxide materials calcined at different temperatures. All the materials, except Meso-Co-150 °C, had a typical spinel Co₃O₄ crystalline pattern according to JCPDS (no. 090418). Increasing heat treatment temperature (250–450 °C) resulted in patterns with sharper diffraction lines, which indicated that the particle grain sizes were increased. Compared to commercial Co₃O₄ sample (C-Co₃O₄), however, Meso-Co-X materials have much smaller grain sizes. Using {311} planes of Co₃O₄ for grain size calculation by the Scherrer equation, the particle grain sizes of Meso-Co-X samples are in the range of 8.25–19.57 nm, while commercial Co₃O₄ has a particle size of 89.25 nm. The PXRD pattern of Meso-Co-150 showed a mixed phase consisting of C₄H₆CoO₄·4H₂O and Co₃O₄. The crystal structure was totally transformed to Co₃O₄ after a heat treatment at 250 °C.

Figure 1b gives the low angle diffraction lines of cobalt oxide samples. Meso-Co-250 and Meso-Co-350 diffracted in the low angle region, indicating the existence of a mesostructure, like other UCT materials.^{18,20} Meso-Co-150 and Meso-Co-450 as well as the commercial Co₃O₄ failed to show a diffraction line in low angle PXRD. The low angle PXRD diffraction line position for Meso-Co-350 shifted to a smaller 2θ value compared to Meso-Co-250, which further confirms the fact that the particle size of UCT materials expands with increasing heat treatment temperature. (According to the model of UCT

materials, low angle diffraction line positions correspond to the average particle size.) Therefore, Meso-Co-450 could still have a mesostructure, but the diffraction line position might shift to a lower angle that is beyond the detection limit.

The change of the nanoparticle sizes upon heat treatment was also observed in TEM analyses (Figure 1c–e). The nature of the particles is a nanoparticle aggregate, the same as other UCT materials. All TEM images were collected with the same magnification for better evaluation of the change of the particle sizes with different heat treatment. With calcination temperature increasing from 250 to 450 °C, the particle size changed from 11.4 to 21.7 nm, which corresponds well with the tendency revealed by low angle PXRD characterization.

3.1.2. N₂ Sorption. Similar to the trend found in PXRD, Barrett–Joyner–Halenda (BJH) desorption pore diameters built up from 1.9 to 17.5 nm with the final heat treatment temperature increasing from 150 to 450 °C, as shown in Figure 2b. The Meso-Co-150 sample demonstrated its nonporous

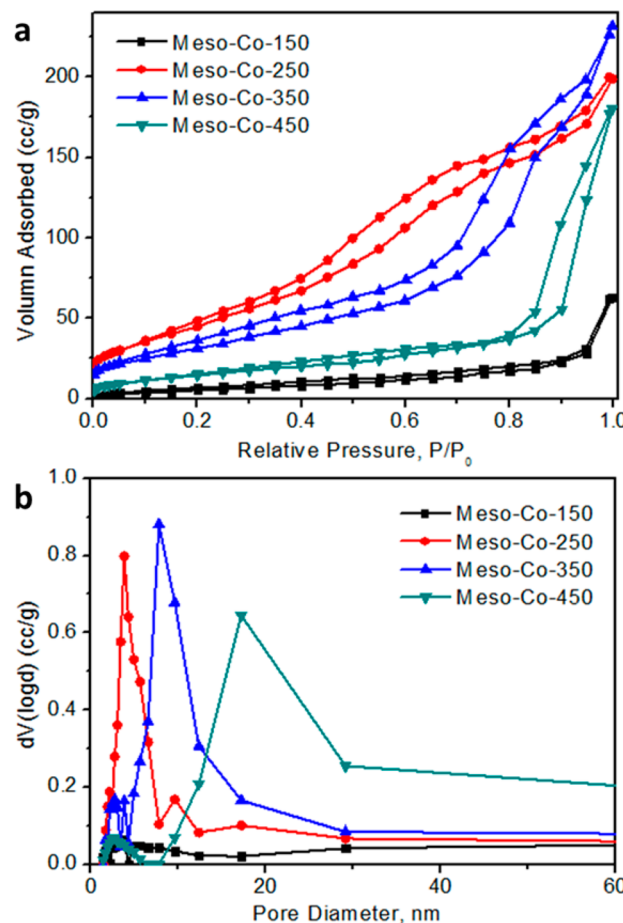


Figure 2. BET measurements: (a) N₂ sorption isotherms and (b) BJH desorption pore size distributions of Meso-Co-X (X = 150, 250, 350, and 450).

nature (type III isotherm) while Meso-Co-250 and Meso-Co-350 showed a characteristic Type IV adsorption isotherm, followed by a Type I hysteresis loop (Figure 2a), suggesting the existence of a regular ordered mesoporous structure.¹⁸ These two materials also have very high surface areas (>100 m² g⁻¹) and large pore volumes (>0.349 cc g⁻¹). Meso-Co-450 showed a further expansion in pore size and the BJH desorption pore size distribution still suggests a uniform porous structure (17.5

Table 1. Structural Parameters and Catalytic Performance of Different Catalysts Discussed in This Manuscript

heat treatment <i>T</i> (°C)	BET surface area (m ² /g)	BJH Des. pore volume (cm ³ /g)	BJH Des. pore diameter (nm)	low angle diffraction position (nm)	crystal structure	<i>T</i> ₁₀₀ ^a
150	22.9	0.10	1.9	<i>b</i>	Co ₃ O ₄ and C ₄ H ₆ CoO ₄ ·4H ₂ O	180 °C
250	181.4	0.35	3.8	9.29	Co ₃ O ₄	-35 °C
350	120.8	0.38	7.7	11.03	Co ₃ O ₄	-60 °C
450	57.9	0.29	17.5	<i>b</i>	Co ₃ O ₄	0 °C

^a*T*₁₀₀: temperature where full conversion of CO to CO₂ takes place. ^bSignifies not applicable.

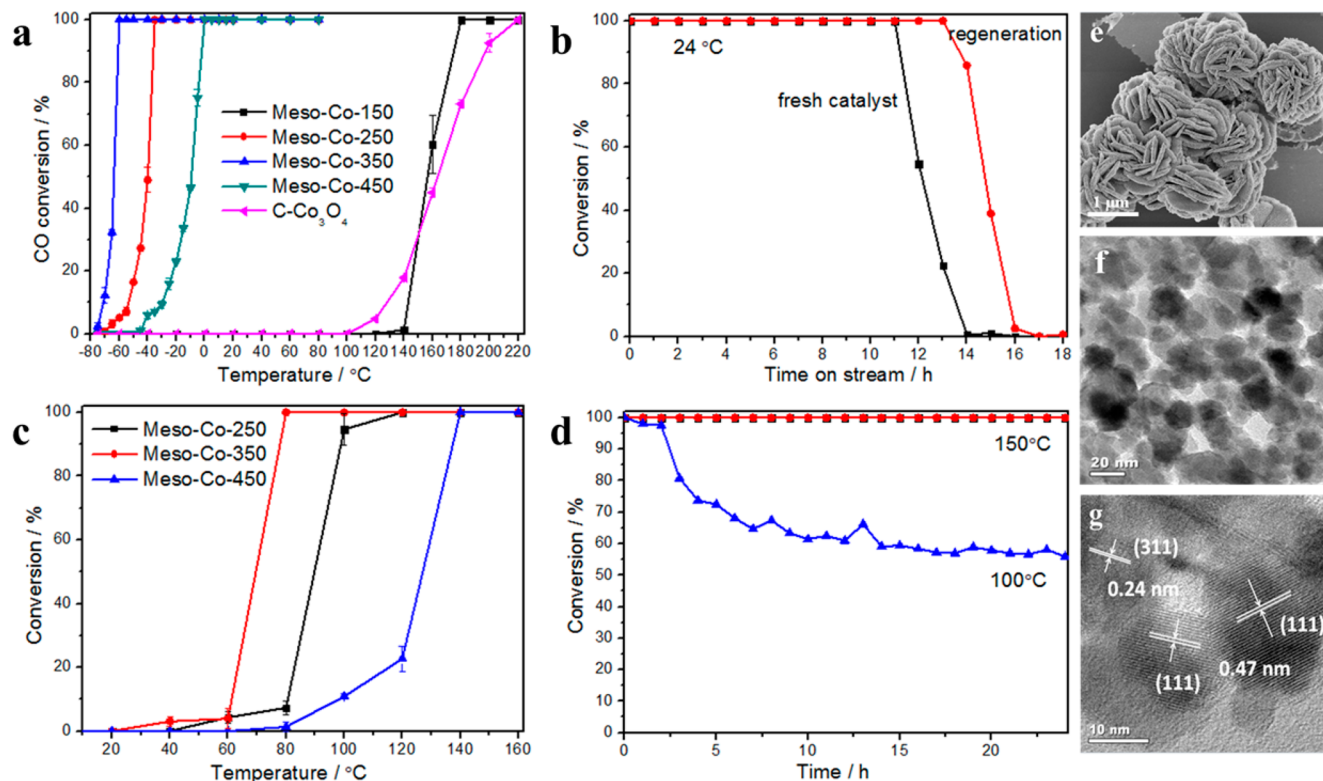


Figure 3. Catalytic performance toward CO oxidation. (a) CO light off of Meso-Co-X (X = 150, 250, 350, and 450) as well as C-Co₃O₄ and (b) long-term durability test of Meso-Co-350 at room temperature under normal conditions (~3–10 ppm of H₂O). (c and d) CO light off plot of Meso-Co-X (X = 250, 350, and 450) and stability test of Meso-Co-350 and Meso-Co-250 under moisture rich conditions (~3% H₂O). (e–g) FE-SEM, TEM, and HR-TEM images of Meso-Co-350 after stability test under normal conditions.

nm). However, the surface area decreased significantly compared with Meso-Co-250 and Meso-Co-350. Such phenomenon proves the successful synthesis of UCT-8 materials whose particle sizes, pore diameters, and pore volumes can be tuned by heat treatment at different temperatures. The BET surface area, BJH pore volume, and other structural parameters are summarized in Table 1.

3.1.3. Electron Microscopy. Morphological properties of mesoporous cobalt oxides were investigated by field emission scanning electron microscope (FE-SEM) and high-resolution transmission electron microscopy (HR-TEM). Figure S1a–d in the Supporting Information shows SEM images of Meso-Co-X (X = 250, 350, 450) samples. The samples are flower-like round particles consisting of nanosize plates. Meso-Co-150 also consists of flower like round particles but fails to show a uniform morphology due to incomplete transformation to the Co₃O₄ phase (see Figure 1a). The pore openings also expanded with heat treatment. In Meso-Co-450, uniform pores can be clearly seen in the images. High-resolution transmission electron microscopy (HR-TEM) images are shown in Figure S1e–g in the Supporting Information. The obtained meso-

porous cobalt oxides with crystalline walls exhibited well-defined lattice fringes. The *d*-spacing values are measured to be 0.28, 0.24, and 0.47 nm, corresponding to {220}, {311}, and {111} planes of the Co₃O₄ spinel structure, respectively. In spinel cobalt oxide, Co³⁺ occupies octahedral sites coordinating with six oxygen atoms while Co²⁺ possesses tetrahedral sites with four neighboring oxygen atoms. Crystallography studies of the spinel cobalt oxide lattice suggest that Co³⁺ is highly populated within {110} planes while {111} planes contain Co²⁺ only.

3.2. CO Oxidation Reaction Activity. Figure 3 shows the catalytic performance toward carbon monoxide oxidation under various conditions of Meso-Co-X samples. Performance of commercial Co₃O₄ (C-Co₃O₄) is also included for comparison. Figure 3a gives the activity behavior under normal conditions (~3–10 ppm of H₂O). Among these materials, Meso-Co-350 was the best catalyst and completely oxidized carbon monoxide at temperatures as low as -60 °C. Meso-Co-250 showed slightly lower activity with the temperature of 100% conversion (*T*₁₀₀) at -35 °C. Compared to Meso-Co-250 and Meso-Co-350, Meso-Co-450 could only oxidize CO

completely at 0 °C. However, its catalytic activity was still much higher than that of the commercial Co_3O_4 , which exhibited no conversion at temperatures below 120 °C and did not fully convert CO to CO_2 until the temperature reached 220 °C. On the other hand, Meso-Co-150 did not start to convert CO until 120 °C and then the conversion increased rapidly and reached 100% at 180 °C. The behavior suggested that the catalyst may undergo phase transformation in the temperature range of 120–180 °C. Since Meso-Co-350 exhibited the best catalytic performance, this material was selected for long-term durability tests. The results are demonstrated in Figure 3b. The catalyst maintains 100% conversion for 11 consecutive hours at room temperature. After 14 h, the sample was totally deactivated and was regenerated under helium flow at 200 °C for 1 h. Upon regeneration the activity was fully recovered and became even better compared with the fresh-prepared sample. No activity loss was observed for 13 h.

CO oxidation under moisture rich conditions (~3% H_2O) was also performed. After sending about 3% moisture into the feed gas stream, T_{100} of the catalysts shifted to higher temperatures (Figure 3c). Meso-Co-350 still exhibited the best performance with 100% conversion at 80 °C. T_{100} of Meso-Co-250 and Meso-Co-450 were 120 and 140 °C, respectively. Stability tests under moisture rich condition are shown in Figure 3d. At 150 °C, both Meso-Co-250 and Meso-Co-350 maintained 100% CO conversion for 24 h. However, at 100 °C, Meso-Co-350 gave 100% conversion initially, then the CO conversion tended to decrease but still remained >50% conversion after 24 h. CO oxidation in moisture rich conditions over metal oxides was previously studied by several other research groups.^{6,11,12,21,22} Xie et al. obtained ~92% conversion at 150 °C with 8.20 vol % H_2O in the gas stream.⁶ Kuo et al. synthesized Co_3O_4 nanoparticles on carbon nanotubes with polymer coatings and reached 100% conversion at 150 °C with ~3% moisture.²² Chen et al. prepared several metal oxides and coated them with hydrophobic polymer PDMS. The best performance in the gas stream containing ~3% moisture was achieved by PDMS coated amorphous manganese oxide, which showed CO conversion of 63% at 100 °C and reached a total conversion at 130 °C.¹¹ Compared to literature findings, the results presented here are promising.

Figure S2 in the Supporting Information shows the PXRD pattern of Meso-Co-150 before and after reaction. The sample was transformed from $\text{C}_4\text{H}_6\text{CoO}_4 \cdot 4\text{H}_2\text{O}$ to a Co_3O_4 spinel phase during the reaction. Also the color of the catalyst changed from pink to black. The decreased O_2 concentration but increased CO_2 concentration detected in the outlet gas at 160 °C indicated the remaining carboxyl groups in the catalyst have been transformed into CO_2 . Similar behavior of carboxyl and nitrate groups removal of UCT materials monitored by TPD was reported.¹⁸ When the temperature was elevated above 160 °C, the residues in the sample started to be removed gradually and thus more active sites were exposed leading to the rapidly developing catalytic activity of Meso-Co-150 in the range of 140–180 °C. Thermogravimetric analysis of the sample confirmed a significant weight loss at around 210 °C in air. Therefore, the complete oxidation of CO can be achieved upon the removal of the residues at around 200 °C.

For other samples (Meso-Co-250, 350, and 450), such transformation during reaction was not observed. The PXRD analysis of the catalysts after reaction showed the same patterns as those before reaction (Figure S3 in the Supporting Information). Morphologies of Meso-Co-350 after stability

test under normal conditions are shown in Figure 3e–g. No obvious morphological change from either FE-SEM or HR-TEM images was observed as compared to the fresh catalyst. The HR-TEM image still displayed clear lattice fringes of Co_3O_4 which confirmed there is no phase transformation or segregation. This result indicated the catalyst was able to maintain its structural integrity and experienced no physical damage throughout the long-term reaction.

3.3. X-ray Photoelectron Spectroscopy (XPS). For Co_3O_4 catalysts, higher surface area can contribute to higher catalytic activity due to more exposed active sites and weakened Co–O bond strength.^{23,24} Since Meso-Co-250 has the highest surface area but is not the most active catalyst (Table 1), the differences of catalytic performances of these materials cannot be solely contributed to effects of surface area. Other factors such as surface properties and metal valence states need to be considered. A useful technology to study the surface chemistry of the catalysts is X-ray photoelectron spectroscopy (XPS). The XPS spectra of Meso-Co-X ($X = 250, 350$, and 450) as well as Meso-Co-350* (Meso-Co-350 after stability tests under normal conditions) are shown in Figure 4. The Co 2p_{3/2} and Co 2p_{1/2} peak positions located at around 780 and 795 eV (Figure 4a) are in good agreement with the presence of Co_3O_4 .^{9,25,26} The Co 2p spectra were further deconvoluted into Co^{2+} and Co^{3+}

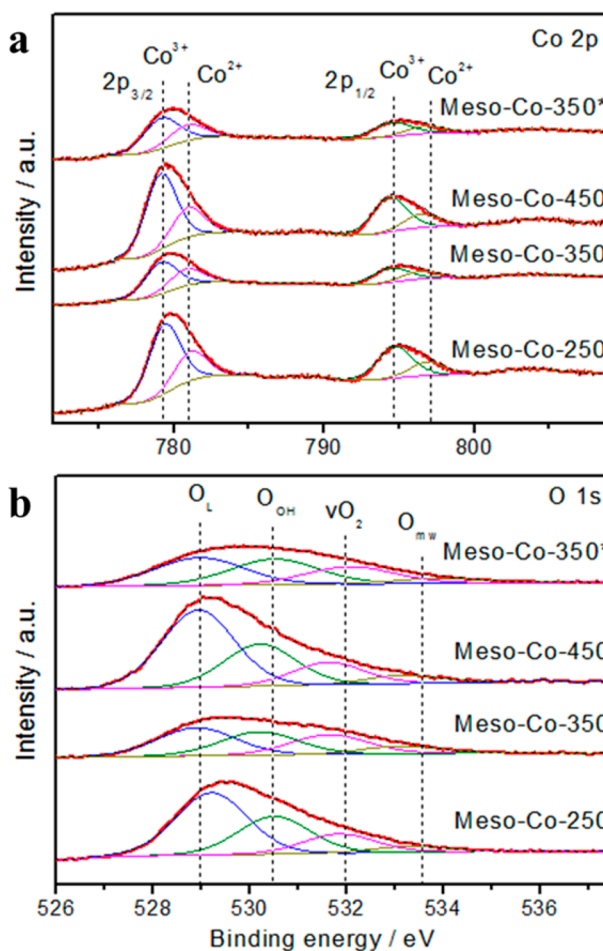


Figure 4. X-ray photoelectron spectroscopy (XPS) analysis: (a) Co 2p and (b) O 1s deconvoluted XPS spectra of mesoporous cobalt oxides (Meso-Co-X; $X = 250, 350, 450$, and 350*). Meso-Co-350* is the deactivated Meso-Co-350 sample after long-term stability tests under normal conditions for 15 h.

signals, respectively, as shown in Figure 4a. Co 2p peaks at binding energies of ~779 and 795 eV are characteristic of Co^{3+} , while the peaks at ~781 and 797 eV correspond to Co^{2+} .^{27–29} Different surface oxygen species have been identified by the deconvoluted O 1s spectrum. The asymmetry of the O 1s peak on higher binding energy side suggested the existence of surface adsorbed oxygen containing species. Specifically, the fitted O 1s spectra displayed four major oxygen contributions with the corresponding peaks centered at ~529, 530, 532, and 533 eV. These bands can be attributed to Co–O bonds (O_L), hydroxyl (O_OH), oxygen vacancies (vO_2), and chemisorbed water (O_mw), respectively. Peak area percentages of these four different oxygen components are listed in Table 2. The $\text{Co}^{2+}/\text{Co}^{3+}$ ratios

Table 2. Summary of Area Percentages of Different Elemental Components Obtained from the Deconvoluted Spectra

sample	% area					
	Co 2p _{3/2}		O 1s			
	Co^{2+}	Co^{3+}	O_mw	vO_2	O_OH	O_L
Meso-Co-250	19.7	46.9	4.7	15.4	30.2	49.7
Meso-Co-350	23.1	43.6	9.5	25.1	29.7	35.8
Meso-Co-450	18.8	47.8	5.6	14.9	28.0	51.5
Meso-Co-350*	22.6	44.0	6.5	23.0	33.9	36.6

of cobalt oxides heated from 250 to 450 °C were calculated to be 0.42, 0.53, and 0.39, respectively, among which Meso-Co-350 had the highest amount of Co^{2+} (23.1%) and exhibited the most abundant oxygen vacancies (25.1%) on the surface. After stability tests, the surface composition of Meso-Co-350 did not change a lot compared to the fresh catalyst, with 22.6% Co^{2+} and 23.0% oxygen vacancies remaining on the surface.

3.4. Redox Properties. Catalysts exhibiting higher activity toward oxidation reaction generally have higher reducibility.^{30,31} H₂-TPR measurements were performed to investigate the difference in redox properties of Meso-Co-X (X = 250, 350, and 450) and C–Co₃O₄ (Figure 5). Integrated peak areas of H₂ consumption at various temperature ranges are summarized in

Table S1 in the Supporting Information. It is controversial in the literature with respect to the TPR spectrum of Co₃O₄. For example, Arnaldy and Moulijin³² reported one broad peak for the reduction of Co₃O₄. However, more commonly, the reduction steps for Co₃O₄ was believed to be a stepwise process via Co₃O₄ → CoO → Co⁰.^{33–36} Luo et al.²³ and Spadaro et al.³⁷ found that the reduction behavior of Co₃O₄ is highly dependent on the dispersion state of cobalt. Large particles of Co₃O₄ were usually reduced to metallic cobalt in a single step while nanoparticles often went through a two-step process. The reduction steps for Co₃O₄ samples presented here were consistent with literature findings. Mesoporous Co₃O₄ with nanoparticle sizes got reduced in a two-step fashion while C–Co₃O₄ was reduced directly to metallic Co due to its relatively large particle size, as discussed in section 3.1. The reduction profiles of mesoporous cobalt oxides started with a sharp peak in the range of 220–300 °C, which can be ascribed to the reduction from Co³⁺ to Co²⁺ (Co₃O₄ → CoO). The subsequent broader reduction peak in the temperature range of 300–480 °C corresponded to the reduction of CoO to metallic Co. Integration of the peak areas in these two regions showed the ratio of the two peaks was close to the calculated stoichiometric ratio of 1:3 (see Table S1 in the Supporting Information). In addition, PXRD patterns of Meso-Co-350 at the two reduction stages are shown in Figure S4 in the Supporting Information, which further confirms the proposed two-step reduction of mesoporous cobalt oxides. When the final heat treatment temperature was increased from 250 to 350 °C, both reduction peaks shifted to lower temperatures, indicating an enhanced reducibility of Meso-Co-350. Hydrogen spillover, structural change, and promoted oxygen mobility are the major possibilities responsible for the enhanced reduction behaviors of base metal oxides.²³ Hydrogen spillover is usually achieved by promoted metal oxides, especially noble metals. The samples presented in this study are pure spinel cobalt oxides without any promoting ions. Therefore, the enhanced oxygen mobility seems to be the only possible reason for the increased reducibility of Meso-Co-350. Further increasing the final temperature to 450 °C (Meso-Co-450) has led to a decrease of reducibility. PXRD and N₂ sorption measurements showed Meso-Co-450 had a larger particle size and smaller surface area as compared with Meso-Co-250 and Meso-Co-350. These factors can account for the decreased reducibility of Meso-Co-450. From H₂-TPR characterization, mesoporous cobalt oxides were found to demonstrate much higher reducibility than C–Co₃O₄. The order of catalysts' reducibility correlates well with their catalytic activities (see section 3.4). Besides the two major peaks in the temperature range of 200–450 °C, there are small peaks below 200 °C. These peaks can be attributed to the reduction of surface oxygen species (O₂[−] or O[−]) adsorbed on oxygen vacancies.^{23,36} Meso-Co-350 had a small broad peak at 128 °C, as compared to Meso-Co-250 which had a smaller peak at around 185 °C. This indicated the heat treatment of UCT-8 from 250 to 350 °C helped generate more oxygen vacancies and increased the reactivity of surface adsorbed oxygen species. The presence of oxygen vacancies was also suggested by XPS (Figure 4) data. Meso-Co-350 had the most abundant surface lattice defects. These defects might enhance lattice oxygen mobility of Meso-Co-350 and further promote its reducibility.

3.5. Reaction Mechanism. 3.5.1. O₂-TPD. XPS and H₂-TPR analyses suggested that oxygen vacancies on catalyst surfaces may have a promotion effect on the redox properties

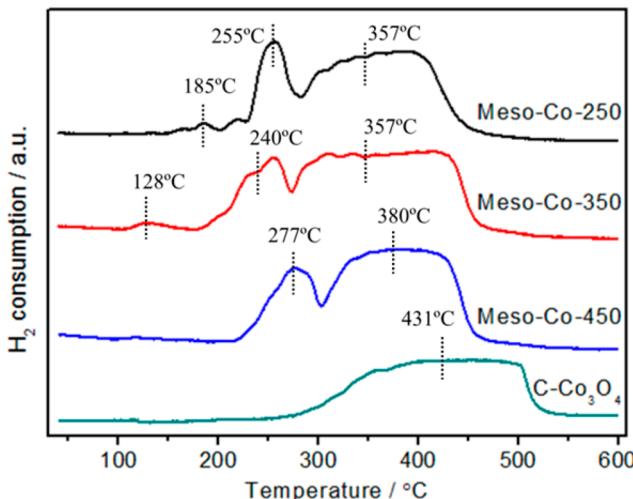


Figure 5. H₂-TPR profiles of mesoporous cobalt oxides (Meso-Co-X; X = 250, 350, and 450) and commercial cobalt oxide (C–Co₃O₄). The measurements were conducted from room temperature to 600 °C (10 °C/min) under a stream of 10% H₂/N₂ with a flow rate of 50 sccm.

and thus catalytic activity. To further investigate the surface defects and lattice oxygen mobility of the catalysts, temperature-programmed desorption (TPD) analyses were performed. Similar to H₂-TPR, different peak areas in the TPD spectra were integrated and the results are summarized in Table S2 in the Supporting Information. Figure 6a presents the O₂-TPD

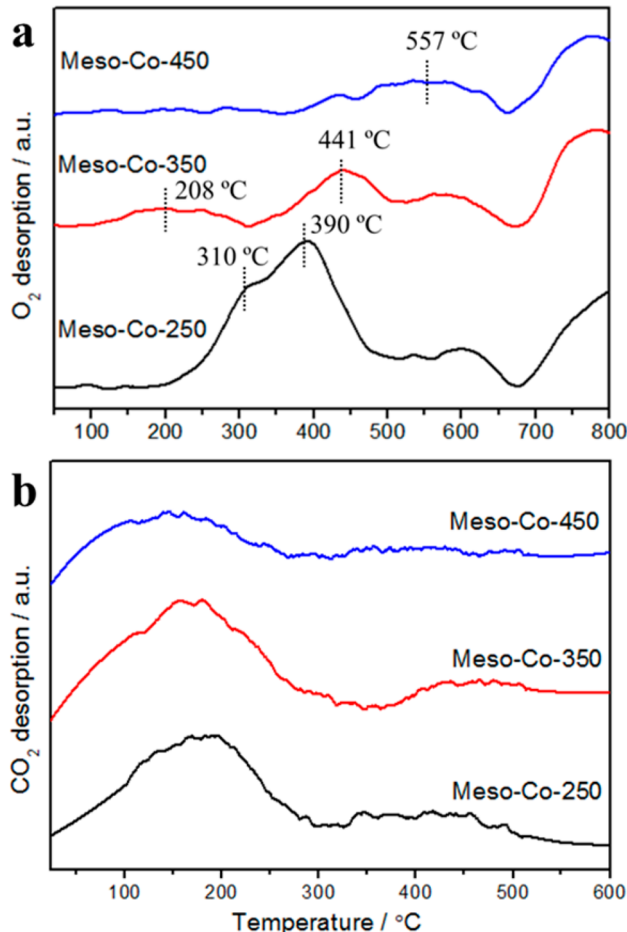


Figure 6. (a) O₂-TPD and (b) CO-TPD profiles of Meso-Co-X ($X = 250, 350$, and 450) samples. The signals were recorded when the samples were heated under Ar (200 sccm) from room temperature to $800\text{ }^{\circ}\text{C}$ with a heating rate of $10\text{ }^{\circ}\text{C}/\text{min}$.

spectra of Meso-Co-X ($X = 250, 350$, and 450) samples. Generally, the surface adsorbed oxygen species undergo the following transformation procedures with electron gain: O₂(ad) \rightarrow O₂[−](ad) \rightarrow O[−](ad) \rightarrow O^{2−}(ad/lattice). O₂(ad) refers to physically adsorbed oxygen, which usually can be removed by purging argon before the analysis. The oxygen adsorbed species of O₂[−](ad) and O[−](ad) are weakly bonded to catalyst surfaces and are easier to desorb. O^{2−}(ad/lattice) is the surface lattice oxygen and is difficult to be extracted. On the basis of results from the literature,^{38–40} the desorption peaks below $350\text{ }^{\circ}\text{C}$ are usually attributed to surface adsorbed O₂[−](ad) and O[−](ad) species. These superficial oxygen species are associated with surface defects. The peaks located at temperatures higher than $350\text{ }^{\circ}\text{C}$ come from the extraction of surface lattice oxygen and bulk lattice oxygen. Therefore, the oxygen desorption peaks with respect to temperature ranges can be classified as follows:

(1) $150\text{--}250\text{ }^{\circ}\text{C}$: desorption of surface adsorbed peroxy species O₂[−](ad),

(2) $280\text{--}340\text{ }^{\circ}\text{C}$: desorption of surface adsorbed monatomic species O[−](ad),

(3) $350\text{--}670\text{ }^{\circ}\text{C}$: desorption of surface lattice oxygen O^{2−}(ad/lattice), and

(4) Beyond $700\text{ }^{\circ}\text{C}$: desorption of bulk lattice oxygen.

As shown in Figure 6a, all samples exhibited a large intense peak above $700\text{ }^{\circ}\text{C}$ due to thermal decomposition of Co₃O₄. Among these catalysts, Meso-Co-250 exhibited a shoulder peak at $310\text{ }^{\circ}\text{C}$ and Meso-Co-350 had a small broad peak centered at around $208\text{ }^{\circ}\text{C}$, referring to the surface adsorbed monatomic species O[−](ad) and peroxy species O₂[−](ad), respectively. The results were consistent with H₂-TPR analysis in which Meso-Co-350 had more reactive surface adsorbed oxygen species than Meso-Co-250. Surface lattice oxygen desorbed in the temperature range of $350\text{--}670\text{ }^{\circ}\text{C}$. With increasing heat treatment temperature of the material from 250 to $450\text{ }^{\circ}\text{C}$, surface lattice oxygen desorbing temperature shifted to higher temperatures ($390 \rightarrow 557\text{ }^{\circ}\text{C}$), and the relative amount of oxygen evolved decreased significantly. Tang et al. prepared CeO₂/Co₃O₄ samples and found their surface areas decreased under high annealing temperatures. They claimed increasing the surface areas of the samples can weaken the Co–O bond and promote lattice oxygen desorption from Co₃O₄.²⁴ The larger surface areas can also enable more lattice oxygen exposed on the surface. Therefore, the decreased surface lattice oxygen mobility of Meso-Co-X calcined from 250 to $450\text{ }^{\circ}\text{C}$ can be attributed to surface area effect. Correlating the findings from O₂-TPD with the catalytic performance, surface defects generation as well as high surface areas improved the catalytic activity of the catalysts for CO oxidation.

3.5.2. CO-TPD. In order to look into the surface oxygen activity of mesoporous cobalt oxides toward CO oxidation, CO-TPD measurements were also conducted. CO₂ desorption spectra in the absence of O₂ after CO adsorption are shown in Figure 6b. All the carbon monoxide adsorbed on the catalyst surface desorbed as carbon dioxide during the heating cycle with no CO signal detected. This indicates that lattice oxygen is involved in CO oxidation and the amount of desorbed CO₂ reveals the quantity of active surface lattice oxygen of the catalyst. CO₂ desorption amount follows the same tendency as CO oxidation catalytic activity: Meso-Co-350 > Meso-Co-250 > Meso-Co-450. Similar as discussed previously, the higher surface area and more lattice defects result in higher lattice oxygen mobility. The presence of oxygen vacancies on Meso-Co-350 acts as a driving force for lattice oxygen migration.⁴¹ This explains the highest activity of Meso-Co-350, even though its surface area is smaller than that of Meso-Co-250. The CO₂ desorption temperatures of various materials are more or less the same ($\sim 170\text{ }^{\circ}\text{C}$), which suggests similar CO₂ desorption rates from catalyst surfaces.

3.6. Deactivation Mechanism. **3.6.1. Fourier Transform-Infrared Spectroscopy (FT-IR).** To understand the deactivation reason, FT-IR tests were conducted on Meso-Co-350 to investigate the difference of the sample before and after deactivation. The spectrum of Meso-Co-350 before the reaction was obtained after the fresh sample was pretreated under He flow at $200\text{ }^{\circ}\text{C}$ for 1 h. After pretreatment, the reaction gas mixture was passed through the catalyst bed for 15 h under normal conditions to ensure complete deactivation, then the IR spectrum was recorded. The sample was tested immediately after each treatment stage. Results are displayed in Figure 7a. Meso-Co-350 before and after deactivation both show two distinctive bands at 565 and 663 cm^{-1} , which originate from the

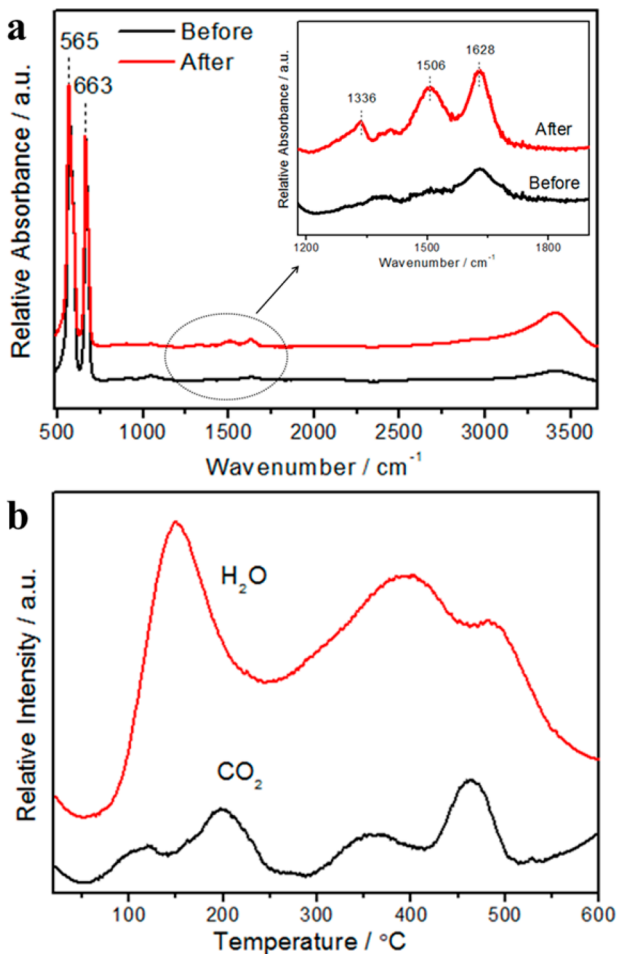


Figure 7. Characterizations of deactivated material: (a) FT-IR spectra of Meso-Co-350 before and after long-term stability tests under normal conditions for 15 h. (b) TPD profiles of Meso-Co-350 after complete deactivation under normal conditions. The desorption profiles were detected under Ar flow (200 sccm) with a heating rate of 10 °C/min.

characteristic stretching vibrations of the Co_3O_4 metal–oxygen bond.⁴²

This indicates that the Co_3O_4 spinel structure remained after long-term reaction. A broad band at around 3400 cm^{-1} corresponds to the stretching vibration of adsorbed molecular water.⁹ As shown in Figure 7a, the deactivated sample exhibits a much more intense water band. Even if the reaction was conducted under normal conditions without using additional water vapor, trace amounts of water ($\sim 3\text{--}10 \text{ ppm}$) present in the feed gas can accumulate on the catalyst. The detailed intensity change of IR bands in the range $1200\text{--}1800 \text{ cm}^{-1}$ was enlarged and is shown in the inset graph. The band at 1628 cm^{-1} is due to the vibration of adsorbed molecular H_2O .⁹ Additionally, the bands at 1336 and 1506 cm^{-1} can be assigned to the bending modes of carbonates, similar to the frequencies reported in the literature.^{18,43,44} After deactivation, the amount of molecular water was increased significantly and carbonates were formed on the catalyst, which might be responsible for the activity decay.

3.6.2. TPD after Deactivation. A TPD test was run on the used Meso-Co-350 after the stability test under normal conditions to identify gases adsorbed on the catalyst surface during the reaction and may explain the possible reasons for the

deactivation. Meso-Co-350 was first purged under the reaction gas mixture for 15 h and then heated under argon flow. Desorbed gases were monitored continuously. The results are displayed in Figure 7b. Strong water signals as well as carbon dioxide peaks were detected. A carbon dioxide desorption peak at around 200°C can be assigned to decomposition of carbonate species formed during the reaction.^{6,45–47} Another major CO_2 peak at around 460°C may correspond to the interaction between surface carbon and lattice oxygen.^{45,46,48} Surface carbon might be formed by CO disproportionation ($2\text{CO} \rightarrow \text{C} + \text{CO}_2$). In the meantime, a significant amount of water was generated during the reaction. Figure 7b shows a sharp peak of water at 150°C indicating moisture accumulation during the reaction. Besides the water desorption peak at 150°C , another broad peak in the $310\text{--}520^\circ\text{C}$ range corresponds to some strongly adsorbed water molecules on the surface.⁶ The TPD results match perfectly with the FT-IR data. They both suggest that the formation of carbonates and increasing water amount might be possible deactivation paths for low temperature CO oxidation.

4. DISCUSSION

In this study, mesoporous cobalt oxides (UCT-8) were successfully synthesized by a recently developed approach.¹⁸ This method involves the use of inverse surfactant (Pluronic P123) micelles. Sol–gel reactions of the metal oxo-clusters were controlled in acidic medium by unique NO_x chemistry. NO_x refers to a wide range of nitric oxides formed by thermal decomposition of the nitrate ion. The formed NO_x are adsorbed on the surface oxo-clusters to prevent uncontrolled condensation and their further decomposition increased the pH of the solution, which yielded oxidation of the oxo-clusters. Finally, the formed metal oxide mesostructure was a result of monodispersed nanoparticle aggregation and the mesopores were formed by connected intraparticle voids. Characterization studies of the as-prepared mesoporous cobalt oxides demonstrated the typical features of UCT materials. One low angle diffraction line and a Type IV adsorption isotherm, indicating a regular mesopore structure with a monomodal pore size distribution. Moreover, during heat treatment, unit cell expansion and pore size enlargement were observed. This unique properties of UCT materials can be readily seen by low angle PXRD (Figure 1b), TEM images (Figure 1c–e) and pore size distribution graphs (Figure 2b). As summarized in Table 1, the pore size increased from 3.8 to 7.7 nm and particle size grown up from 9.29 to 11.03 nm with increasing thermal treatment temperature from 250 to 350°C . Such control of particle growth and pore size distribution by thermal treatment is unexpected for conventional mesoporous transition metal oxides.⁴⁹ A thermal treatment stage at 250°C is required to completely transform the materials to Co_3O_4 spinel phase.

The CO oxidation catalytic activity over metal oxide catalysts is believed to be closely associated with surface area, lattice defects, lattice oxygen mobility, crystallinity, and the valence state of cations.^{41,50–53} Here we use several characterization techniques to examine the structural properties of the materials and correlate with their catalytic behavior. Deconvoluted O 1s and Co 2p peaks from XPS analysis indicated that Meso-Co-350 have the most abundant oxygen vacancies as well as the highest $\text{Co}^{2+}/\text{Co}^{3+}$ ratio (Figure 4). This is reasonable considering the overall surface charge neutrality. The Co_3O_4 spinel structure contains both Co^{2+} and Co^{3+} cations. With higher surface concentration of Co^{2+} , oxygen deficiency is

required to compensate for the positive charge loss on the surface and thus the formation of surface oxygen vacancies is favored. H₂-TPR measurements give the information about the reducibility of the catalysts. Figure 5 indicates Meso-Co-350 is the most reducible catalyst. Reduction peaks below 200 °C are assigned to the reduction of surface adsorbed oxygen on oxygen vacancies. Again, Meso-Co-350 exhibited the largest quantity of surface defects. According to the literature,^{38,54} the more susceptible a metal oxide is to be reduced, the easier it is to generate oxygen vacancies. This agrees with our findings in which Meso-Co-350 not only shows the greatest reducibility but also generates the largest amount of oxygen vacancies. This has been further evidenced by O₂-TPD measurements (Figure 6a). Meso-Co-350 had a broad O₂ desorption peak at 208 °C, which was ascribed to desorption of surface adsorbed peroxy species O₂⁻(ad). Correlating these findings with the catalytic activity tests, surface lattice defects enhance the activity of catalysts toward CO oxidation. Figure 6b shows CO-TPD spectra of different catalysts. All the carbon monoxide adsorbed on catalyst surfaces was desorbed as CO₂. Since lattice oxygen was the only oxygen source, the participation of lattice oxygen in the reaction was confirmed. On the basis of these findings, the reaction here is believed to proceed via the Mars-van Krevelen mechanism, in which the gas phase oxygen is exchanged with lattice oxygen.^{55–57} Similar to the mechanisms reported in the literature,^{23,45,46,58} the oxidation of carbon monoxide involves a redox cycle between Co²⁺ and Co³⁺. Carbon monoxide is first adsorbed on the catalyst. The adsorbed CO extracts the neighboring lattice oxygen and desorbs as CO₂, leaving the catalyst surface with an oxygen vacancy. The partially reduced site can be replenished by gas phase oxygen and acts as active site for O₂ dissociation. Since O₂ dissociation is an endothermic process,⁵⁸ it is not a dominant step in a low temperature reaction. The rate-determining step for CO oxidation is the reaction between CO and lattice oxygen, which generates an oxygen vacancy.^{41,58,59} The presence of surface oxygen vacancies can promote the lattice oxygen diffusion from the bulk to the surface and facilitates the adsorption–desorption process of the gas phase species.⁶⁰ That leads to an enhanced catalytic performance. Typically, the generation of surface oxygen vacancies involves lattice distortion caused by incorporation of other metals.^{23,34,60,61} In the present study, lattice defects can simply be tuned by thermal treatment, which provides an alternative way to design redox active catalysts. Besides the promotion role of oxygen vacancies, surface area is another important factor in CO oxidation reactions. XPS results suggest that the amount of oxygen vacancies on Meso-Co-250 and Meso-Co-450 is on the same level, thus the activity difference can be mainly attributed to surface area differences. Increasing the calcination temperature from 250 to 450 °C significantly decreased the surface area from 181.4 to 57.9 m²/g (see Table 1). As more oxygen is exposed on the surface, Meso-Co-250 exhibited much higher lattice oxygen mobility, as indicated in O₂-TPD and CO-TPD measurements. This accounts for the higher activity of Meso-Co-250 than Meso-Co-450. Also, the presence of monatomic species O⁻(ad) on Meso-Co-250 is suggested by the small peak at 185 °C (H₂-TPR spectrum) and the shoulder peak at 310 °C (O₂-TPD spectrum). This kind of adsorbed oxygen species might also improve the catalytic activity.

Several possible deactivation mechanisms for CO oxidation reactions were proposed in the literature. In the previous studies, the adsorbed CO on the surface extracts the adjacent

lattice oxygen while the generated oxygen vacancy can be reoxidized by gas phase oxygen or further reduced by gas phase CO. If the reduction process proceeds faster than reoxidation, the catalyst surface will be irreversibly reduced causing deactivation.⁴⁶ However, this deactivation mechanism is not supported by the XPS measurements. In Figure 4, Meso-Co-350 after the stability test has almost the same surface composition as that of the fresh catalyst (0.51 Co²⁺/Co³⁺ ratio versus 0.53 for fresh sample). In addition, this deactivation mechanism has not been reported for CO oxidation activity decay over Co₃O₄ at room temperature. Another possible mechanism of deactivation could be the surface reconstruction of the cobalt oxide, in which the coordination of the surface cobalt ions is changed without changing the oxidation state, making initially active cobalt ions unavailable for CO adsorption.⁴⁷ Given that the catalytic activity can be fully restored by heating the catalyst at 200 °C under helium flow (see section 3.2), surface reconstruction may not be responsible for the activity decay. Such kind of reconstruction should not be recovered under an inert atmosphere at a mild temperature. Furthermore, this deactivation mechanism cannot explain why deactivation occurs slowly at higher temperatures. In long-term stability tests, Meso-Co-350 was deactivated after 11 h online reaction under normal conditions (~3–10 ppm of H₂O). The conversion efficiency dropped quickly after the start of deactivation. However, when the reaction temperature was raised to 100 °C, the deactivation rate decreased dramatically. The catalyst still showed more than 50% conversion after 24 h even under moisture saturated conditions (~3% H₂O). At 150 °C, no activity loss was observed throughout 24 h of each run. More commonly, the deactivation was believed to occur when the active sites are blocked by carbonates, molecular adsorbed water, or hydroxyl groups.^{21,62} This blocking effect is consistent with the experimental results. Figure 7b shows a TPD study for deactivated Meso-Co-350, H₂O, and CO₂ desorption peaks at various temperature ranges were detected. Since the catalyst activity can be fully restored by heating under He at 200 °C, the desorption peaks beyond 300 °C due to surface carbon and strongly adsorbed water cannot account for the activity decay. Water accumulation desorbed at 150 °C should be the main reason for deactivation. The small amounts of CO₂ desorbed at 200 °C suggest that carbonate species formation also contributes to the loss of activity. FT-IR data (Figure 7a) also indicate formation of carbonates and accumulation of moisture on the deactivated catalyst. Deconvoluted O 1s spectra (Figure 4b) show that the deactivated Meso-Co-350 contains less molecular adsorbed water than the fresh sample (6.5% compared to 9.5%). This is because the fresh sample was tested without any pretreatment. Pretreatment under inert gas can yield a clean catalyst surface, which should have much less moisture content than the deactivated sample, as evidenced by FT-IR measurements. To summarize, the accumulated moisture as well as carbonates can block the active sites on the catalyst surface and lead to the activity loss. At higher temperatures (>100 °C) water poisoning is largely suppressed and the catalyst can maintain 100% conversion for 24 h at 150 °C even under moisture rich conditions (~3% H₂O). Therefore, the deactivation of mesoporous cobalt oxide results from the blocking effects by water and carbonate species.

5. CONCLUSION

Mesoporous cobalt oxides (UCT-8) were successfully synthesized by a one step sol–gel process using a recently developed

approach. The approach was based on an inverse surfactant micelle. Characterization of the materials demonstrated typical features of UCT materials. The presence of one low angle diffraction line and a Type IV sorption isotherm indicated a regular mesoporous structure with a uniform pore size distribution. Unit cell expansion and pore size enhancement with increasing heat treatment temperature from 150 to 450 °C was observed by PXRD, BET, FE-SEM, and HR-TEM.

The catalytic performance of the catalysts followed the order: Meso-Co-350 > Meso-Co-250 > Meso-Co-450 > Meso-Co-150 > C-Co₃O₄. Meso-Co-350 exhibited the best catalytic behavior with T_{100} of -60 °C under normal conditions (~3–10 ppm of H₂O) and T_{100} of 80 °C under moisture rich conditions (~3% H₂O). The activity order correlated well with the reducibility and lattice oxygen mobility of the catalysts as indicated by TPR and CO-TPD. XPS and O₂-TPD indicated Meso-Co-350 had the most abundant surface oxygen vacancies, which accounts for its promoted catalytic activity. Furthermore, high surface area also contributed to enhanced catalytic activity of Meso-Co-X compared with C-Co₃O₄. Accumulated water and carbonates are proposed to be responsible for the deactivation of the catalysts based on FT-IR and TPD results. The understanding of the effect of lattice defects and surface area on CO oxidation activity and the deactivation mechanism is crucial for continuous improvement of nonprecious metal oxide catalysts toward CO oxidation.

■ ASSOCIATED CONTENT

Supporting Information

Electron microscopy images, characterization of the materials after CO oxidation reactions, PXRD patterns of Meso-Co-350 at different reduction steps, and calculations of the CO conversion and the water amount in the gas stream. This material is available free of charge via the Internet at <http://pubs.acs.org>.

■ AUTHOR INFORMATION

Corresponding Author

*E-mail: steven.suib@uconn.edu.

Notes

The authors declare no competing financial interest.

■ ACKNOWLEDGMENTS

We thank Dr. Heng Zhang for his assistance in XPS analysis and Dr. Frank Galasso for many helpful discussions. This work was funded by the U.S. Department of Energy, Office of Basic Energy Sciences, Division of Chemical, Biological and Geological Sciences under grant DE-FG02-86ER13622.A000.

■ REFERENCES

- (1) Taylor, S.; Rhodes, C. *Catal. Lett.* **2005**, *101*, 31–33.
- (2) Thormählen, P.; Skoglundh, M.; Fridell, E.; Andersson, B. *J. Catal.* **1999**, *188*, 300–310.
- (3) Cargnello, M.; Gentilini, C.; Montini, T.; Fonda, E.; Mehraeen, S.; Chi, M.; Herrera-Collado, M.; Browning, N. D.; Polizzi, S.; Pasquato, L. *Chem. Mater.* **2010**, *22*, 4335–4345.
- (4) Yamaura, H.; Moriya, K.; Miura, N.; Yamazoe, N. *Sens. Actuators, B* **2000**, *65*, 39–41.
- (5) Haruta, M.; Kobayashi, T.; Sano, H.; Yamada, N. *Chem. Lett.* **1987**, 405–408.
- (6) Xie, X.; Li, Y.; Liu, Z.-Q.; Haruta, M.; Shen, W. *Nature* **2009**, *458*, 746–749.
- (7) Saalfrank, J. W.; Maier, W. F. *Angew. Chem., Int. Ed.* **2004**, *43*, 2028–2031.
- (8) Guo, Y.; Ren, Z.; Xiao, W.; Liu, C.; Sharma, H.; Gao, H.; Mhadeshwar, A.; Gao, P.-X. *Nano Energy* **2013**, *2*, 873–881.
- (9) Jia, C.-J.; Schwickardi, M.; Weidenthaler, C.; Schmidt, W.; Korhonen, S.; Weckhuysen, B. M.; Schüth, F. *J. Am. Chem. Soc.* **2011**, *133*, 11279–11288.
- (10) Wang, C.; Yin, H.; Dai, S.; Sun, S. *Chem. Mater.* **2010**, *22*, 3277–3282.
- (11) Chen, C.-H.; Njagi, E. C.; Sun, S.-P.; Genuino, H.; Hu, B.; Suib, S. L. *Chem. Mater.* **2010**, *22*, 3313–3315.
- (12) Hou, X.-D.; Wang, Y.-Z.; Zhao, Y.-X. *Catal. Lett.* **2008**, *123*, 321–326.
- (13) Kresge, C.; Leonowicz, M.; Roth, W.; Vartuli, J.; Beck, J. *Nature* **1992**, *359*, 710–712.
- (14) Poyraz, A. S.; Biswas, S.; Genuino, H. C.; Dharmarathna, S.; Kuo, C. H.; Suib, S. L. *ChemCatChem.* **2013**, *5*, 920–930.
- (15) De Vos, D. E.; Dams, M.; Sels, B. F.; Jacobs, P. A. *Chem. Rev.* **2002**, *102*, 3615–3640.
- (16) Wu, Z.; Zhao, D. *Chem. Commun.* **2011**, *47*, 3332–3338.
- (17) Soler-Illia, G. J.; Crepaldi, E. L.; Grossi, D.; Sanchez, C. *Curr. Opin. Colloid Interface Sci.* **2003**, *8*, 109–126.
- (18) Poyraz, A. S.; Kuo, C.-H.; Biswas, S.; King'ondu, C. K.; Suib, S. L. *Nat. Commun.* **2013**, *4*, 2952.
- (19) Grossi, D.; Cagnol, F.; Soler-Illia, G. d. A.; Crepaldi, E. L.; Amenitsch, H.; Brunet-Bruneau, A.; Bourgeois, A.; Sanchez, C. *Adv. Funct. Mater.* **2004**, *14*, 309–322.
- (20) Poyraz, A. S.; Kuo, C.-H.; Kim, E.; Meng, Y.; Seraji, M. S. I.; Suib, S. L. *Chem. Mater.* **2014**, *26*, 2803–2813.
- (21) Njagi, E. C.; Chen, C.-H.; Genuino, H.; Galindo, H.; Huang, H.; Suib, S. L. *Appl. Catal., B* **2010**, *99*, 103–110.
- (22) Kuo, C.-H.; Li, W.; Song, W.; Luo, Z.; Poyraz, A.; Guo, Y.; Ma, A. W.; Suib, S. L.; He, J. *ACS Appl. Mater. Interfaces* **2014**, *6*, 11311–11317.
- (23) Luo, J.-Y.; Meng, M.; Li, X.; Li, X.-G.; Zha, Y.-Q.; Hu, T.-D.; Xie, Y.-N.; Zhang, J. *J. Catal.* **2008**, *254*, 310–324.
- (24) Tang, C.-W.; Kuo, C.-C.; Kuo, M.-C.; Wang, C.-B.; Chien, S.-H. *Appl. Catal., A* **2006**, *309*, 37–43.
- (25) NIST XPS Database, *X-ray Photoelectron Spectroscopy Database* 20, version 3.0; National Institute of Standards and Technology: Gaithersburg, MD, <http://srdata.nist.gov/XPS>.
- (26) Natile, M. M.; Glisenti, A. *Chem. Mater.* **2002**, *14*, 3090–3099.
- (27) Ren, Z.; Guo, Y.; Zhang, Z.; Liu, C.; Gao, P.-X. *J. Mater. Chem. A* **2013**, *1*, 9897–9906.
- (28) Ding, Y.; Zhu, L.; Huang, A.; Zhao, X.; Zhang, X.; Tang, H. *Catal. Sci. Technol.* **2012**, *2*, 1977–1984.
- (29) Ernst, B.; Bensaddik, A.; Hilaire, L.; Chaumette, P.; Kienemann, A. *Catal. Today* **1998**, *39*, 329–341.
- (30) Shan, W.; Shen, W.; Li, C. *Chem. Mater.* **2003**, *15*, 4761–4767.
- (31) Gupta, A.; Hegde, M.; Priolkar, K.; Waghmare, U.; Sarode, P.; Emura, S. *Chem. Mater.* **2009**, *21*, 5836–5847.
- (32) Arnoldy, P.; Moulijn, J. A. *J. Catal.* **1985**, *93*, 38–54.
- (33) Wang, C.-B.; Tang, C.-W.; Gau, S.-J.; Chien, S.-H. *Catal. Lett.* **2005**, *101*, 59–63.
- (34) Kang, M.; Song, M. W.; Lee, C. H. *Appl. Catal., A* **2003**, *251*, 143–156.
- (35) Liotta, L.; Di Carlo, G.; Pantaleo, G.; Venezia, A.; Deganello, G. *Appl. Catal., B* **2006**, *66*, 217–227.
- (36) Xue, L.; Zhang, C.; He, H.; Teraoka, Y. *Appl. Catal., B* **2007**, *75*, 167–174.
- (37) Spadaro, L.; Arena, F.; Granados, M.; Ojeda, M.; Fierro, J.; Frusteri, F. *J. Catal.* **2005**, *234*, 451–462.
- (38) Fei, Z.; He, S.; Li, L.; Ji, W.; Au, C.-T. *Chem. Commun.* **2012**, *48*, 853–855.
- (39) Wang, Y.-Z.; Zhao, Y.-X.; Gao, C.-G.; Liu, D.-S. *Catal. Lett.* **2008**, *125*, 134–138.
- (40) Liu, Q.; Wang, L.-C.; Chen, M.; Cao, Y.; He, H.-Y.; Fan, K.-N. *J. Catal.* **2009**, *263*, 104–113.

- (41) Liu, Y.; Wen, C.; Guo, Y.; Lu, G.; Wang, Y. *J. Mol. Catal. A: Chem.* **2010**, *316*, 59–64.
- (42) Wang, Y.-Z.; Zhao, Y.-X.; Gao, C.-G.; Liu, D.-S. *Catal. Lett.* **2007**, *116*, 136–142.
- (43) Pollard, M. J.; Weinstock, B. A.; Bitterwolf, T. E.; Griffiths, P. R.; Piers Newbery, A.; Paine, J. B., III *J. Catal.* **2008**, *254*, 218–225.
- (44) Grillo, F.; Natile, M. M.; Glisenti, A. *Appl. Catal., B* **2004**, *48*, 267–274.
- (45) Jansson, J. *J. Catal.* **2000**, *194*, 55–60.
- (46) Jansson, J.; Skoglundh, M.; Fridell, E.; Thormählen, P. *Top. Catal.* **2001**, *16*, 385–389.
- (47) Jansson, J.; Palmqvist, A. E.; Fridell, E.; Skoglundh, M.; Österlund, L.; Thormählen, P.; Langer, V. *J. Catal.* **2002**, *211*, 387–397.
- (48) Tang, S.; Lin, J.; Tan, K. *Catal. Lett.* **1998**, *51*, 169–175.
- (49) Lee, J.; Orilall, M. C.; Warren, S. C.; Kamperman, M.; DiSalvo, F. J.; Wiesner, U. *Nat. Mater.* **2008**, *7*, 222–228.
- (50) Özcar, M.; Poyraz, A. S.; Genuino, H. C.; Kuo, C.-H.; Meng, Y.; Suib, S. L. *Appl. Catal., A* **2013**, *462*, 64–74.
- (51) Lin, H.-K.; Chiu, H.-C.; Tsai, H.-C.; Chien, S.-H.; Wang, C.-B. *Catal. Lett.* **2003**, *88*, 169–174.
- (52) Tüysüz, H.; Comotti, M.; Schüth, F. *Chem. Commun.* **2008**, 4022–4024.
- (53) Hu, L.; Sun, K.; Peng, Q.; Xu, B.; Li, Y. *Nano Res.* **2010**, *3*, 363–368.
- (54) Li, P.; He, C.; Cheng, J.; Ma, C. Y.; Dou, B. J.; Hao, Z. P. *Appl. Catal., B* **2011**, *101*, 570–579.
- (55) Luo, J.; Zhang, Q.; Garcia-Martinez, J.; Suib, S. L. *J. Am. Chem. Soc.* **2008**, *130*, 3198–3207.
- (56) Makwana, V. D.; Son, Y.-C.; Howell, A. R.; Suib, S. L. *J. Catal.* **2002**, *210*, 46–52.
- (57) Homer, C.; Saminda, D.; Eric, C.; Michael, C.; Steven, L. *J. Phys. Chem. C* **2012**, *116*, 12066–12078.
- (58) Shapovalov, V.; Metiu, H. *J. Catal.* **2007**, *245*, 205–214.
- (59) Kim, H. Y.; Lee, H. M.; Henkelman, G. *J. Am. Chem. Soc.* **2012**, *134*, 1560–1570.
- (60) Merino, N. A.; Barbero, B. P.; Grange, P.; Cadús, L. E. *J. Catal.* **2005**, *231*, 232–244.
- (61) Li, J.; Lu, G.; Wu, G.; Mao, D.; Wang, Y.; Guo, Y. *Catal. Sci. Technol.* **2012**, *2*, 1865–1871.
- (62) Xia, G.; Yin, Y.; Willis, W.; Wang, J.; Suib, S. *J. Catal.* **1999**, *185*, 91–105.